Putative fossils of chemotrophic microbes preserved in seep carbonates from Vestnesa Ridge, off NW Svalbard

Tobias Himmler[1,*], Antoine Crémière[2], Daniel Birgel[3], Richard Wirth[4], Victoria J. Orphan[2], Kalle Kirsimäe[5], Jochen Knies[1,6], Jörn Peckmann[3], and Aivo Lepland[1,5,6]

[1]Geological Survey of Norway, Post box 6315 Torgarden, 7491 Trondheim, Norway

[2]Division of Geological and Planetary Sciences, California Institute of Technology, Pasadena, CA, USA

[3]Institut für Geologie, Zentrum für Erdsystemforschung und Nachhaltigkeit, Universität Hamburg, 20146 Hamburg, Germany

[4]GeoForschungsZentrum Potsdam, 3.5 Surface Geochemistry, Telegrafenberg, 14473 Potsdam, Germany

[5]Department of Geology, Tartu University, 50411 Tartu, Estonia

[6]CAGE – Centre for Arctic Gas Hydrate, Environment and Climate, Department of Geosciences, UiT The Arctic University of Norway, 9037 Tromsø, Norway

[*]Email: ollap@web.de

ABSTRACT

The microbial key players at methane seeps are methanotrophic archaea and sulfate-reducing bacteria. They form spherical aggregates and co-jointly mediate the sulfate-dependent anaerobic oxidation of methane (SD–AOM: $CH_4 + SO_4^{2-} \rightarrow HCO_3^- + HS^- + H_2O$), thereby inducing the precipitation of authigenic seep carbonates. While seep carbonates constitute valuable archives for molecular fossils of SD–AOM-mediating microbes, no microfossils have been identified as AOM-aggregates to date. This study reports clustered spherical

microstructures engulfed in ^{13}C-depleted aragonite cement (δ^{13}C values as low as −33‰) of Pleistocene seep carbonates. The clusters comprise Mg-calcite spheres between ~5 µm (single spheres) to ~30 µm (clusters) in diameter. Scanning and transmission electron microscopy revealed a porous nanocrystalline fabric in the core area of the spheres, surrounded by one or two concentric layers of Mg-calcite crystals. *In situ* measured sphere δ^{13}C values as low as −42‰ indicate methane-derived carbon as dominant carbon source. The size and concentric layering of the spheres resembles mineralized aggregates of natural ANME-2 archaea surrounded by one or two layers of sulfate-reducing bacteria. Abundant carbonate-bound ^{13}C-depleted lipid biomarkers of archaea and bacteria indicative for the ANME-2-*Desulfosarcina/Desulfococcus* consortium agree with SD–AOM-mediating microbes as critical agents of carbonate precipitation. Given the morphological resemblance in concert with negative *in situ* δ^{13}C values and abundant SD–AOM-diagnostic biomarkers, the clustered spheres likely represent fossils of SD–AOM-mediating microbes.

INTRODUCTION

In ocean sediments where ascending methane and downward seawater sulfate flux meet at the sulfate–methane transition, microbial consortia of anaerobic methanotrophic archaea (ANME) and sulfate-reducing bacteria (SRB) co-jointly mediate the sulfate–dependent anaerobic oxidation of methane (Boetius et al., 2000). Authigenic seep carbonates precipitate as consequence of SD–AOM-induced bicarbonate production and often preserve ANME/SRB-specific molecular fossils (e.g. Aloisi et al., 2002; Peckmann and Thiel, 2004). Yet, unambiguous ANME/SRB body fossils have not been identified in seep carbonates to date (Shapiro, 2004; Bailey et al., 2010; Suess, 2018). This is puzzling because seep sediments contain up to 10^{10} ANME/SRB consortia per 1 cm^3 and seep carbonates contain 100's of ANME/SRB aggregates per mg wet weight (Marlow et al 2014; Knittel et al., 2018). However, cellular microbial

remnants often resemble natural abiogenic structures, which makes it difficult to ascribe a biogenic origin to microstructures observed in rocks (e.g. Rouillard et al., 2021).

This study reports spherical microstructures in seep carbonates sampled from an active methane seep on Vestnesa Ridge, NW Svalbard (Fig. 1). Bulk-rock lipid biomarker analyses confirm that carbonate precipitation was induced by chemotrophic microbial consortia of SD–AOM-mediating ANME/SRB aggregates. The microstructures reported here resemble mineralized forms of the natural ANME/SRB aggregates that have induced early diagenetic carbonate precipitation. *In situ* microstructure analyses revealed that the structures comprise ^{13}C-depleted Mg-calcite engulfed in ^{13}C-depleted aragonite cement.

METHODS

Carbonates were sampled from the seafloor using a remotely operated vehicle (Fig. 1). Mineralogical compositions of the carbonates were determined by X-ray diffraction. Petrographic thin sections were prepared from epoxy-fixed slabs and examined using optical and scanning electron microscopy (SEM; Fig. 2; Fig. 1 DR1). Lipid biomarkers were extracted from two carbonate rock samples after decalcification; biomarkers and their compound-specific carbon isotope compositions were analyzed using coupled gas chromatography–mass spectrometry. Microstructure cross sections were studied using transmission electron microscopy (TEM) on electron-transparent foils (Wirth, 2009). Chemical composition was analyzed using energy dispersive X-ray analysis (EDX) by TEM. Carbon isotopes of one representative microstructure were analyzed *in situ* by nanoscale secondary ion mass spectrometry (nanoSIMS) on a TEM–foil (Fig. 3). NanoSIMS data were calibrated against repeated standard measurements (Ceramacast 905) with a known $\delta^{13}C$ value (−27.9‰; House, 2015). The $\delta^{13}C$ values were corrected for instrumental bias and quasi-simultaneous arrival (QSA) effect on secondary carbon

ions (Slodzian et al., 2004) (see Figs. 2,3 DR1). All $\delta^{13}C$ values are reported in per mill (‰) relative to VPDB (Vienna Peedee belemnite). For detailed methods see GSA Data Repository[1].

MICROSTRUCTURE COMPOSITION AND BIOMARKERS

The carbonates constitute intraformational breccias of microcrystalline Mg-calcite and aragonite cemented sediment clasts, cemented by pore-filling aragonite. Previously, uranium–thorium dating of the pore-filling aragonite yielded late Pleistocene ages from ~20–18 ka (sample P1606001) and ~28 ka (sample P1606002; Himmler et al., 2019). Thin section microscopy revealed clustered spheres engulfed in the pore-filling aragonite (Fig. 2A; Figs. 1,4 DR1). The clusters range in diameter from ~5 µm (single sphere) to ~30 µm (cluster; Fig. 2B,E,F). Cross-sections through individual spheres reveal that they comprise one or two ~1 to 2 µm wide concentric Mg-calcite layers surrounding interior portions of porous nanometer-sized crystals (Fig. 2C,D,G). The contact to the surrounding aragonite is sharp. Six nanoSIMS $\delta^{13}C$ spot analyses were obtained from the interior portion of one representative sphere (Fig. 3A); after QSA correction, the $\delta^{13}C$ values ranged between −42 to –24‰ (Fig. 3B; data file DR2).

The carbonates contain similar proportions of ^{13}C-depleted archaeal and bacterial lipid biomarkers including the diagnostic SD–AOM biomarker crocetane (data file DR2). Archaeol and *sn*2-hydroxyarchaeol are the most abundant archaeal biomarkers (1214 to 4463 ng per g rock), exhibiting $\delta^{13}C$ values from −113 to −108‰. Phytanol and phytanyl monoethers are also prominent (79 to 352 ng per g rock), revealing $\delta^{13}C$ values from −102 to −91‰. The *iso*- and *anteiso*-$C_{15:0}$ fatty acids (382 to 809 ng) are the most abundant bacterial biomarkers, yielding $\delta^{13}C$ values from –75 to –69‰ (Fig. 3B).

DISCUSSION

Carbonate precipitation environment and microstructure preservation

Previously reported negative carbonate $\delta^{13}C$ values as low as −33‰ for the pore-filling aragonite point to SD–AOM-induced carbonate precipitation (Himmler et al., 2019). Persistent methane flux stimulates SD–AOM which results in enhanced Mg-calcite and aragonite precipitation at seeps due to increased alkalinity near the sediment–water interface (Luff et al., 2004). Detection of calcium, oxygen, and magnesium, and lack of significant strontium within the microstructures together with rhombohedral diffraction pattern agrees with a calcite mineralogy (Fig. 2; data file DR2). Zhang et al. (2012) put forward that relatively high dissolved HS^- concentration lowers the dehydration energy of magnesium–water complexes in methane seep pore fluids, thus promoting Mg^{2+} incorporation into calcite (see also Lu et al., 2012). Relatively high HS^- concentrations are expected in environments dominated by SD–AOM. It is also known that fluids with elevated carbonate alkalinity stimulate carbonate precipitation on negatively charged extracellular polymeric substances (EPS) of microbial mats (e.g. Braissant et al., 2007). Likewise, EPS mineralization of SD–AOM-mediating aggregates may occur when enhanced HCO_3^- production increases the local alkalinity beyond carbonate saturation during persistent methane flux. It has been shown that calcifying microbial mats of methanotrophic archaea and sulfate-reducing bacteria facilitate the growth of authigenic carbonate build-ups consisting of Mg-calcite and aragonite at methane seeps (Michaelis et al., 2002; Reitner et al., 2005). At seeps, active SD–AOM results in coeval high carbonate alkalinity and HS^- concentrations. This may induce Mg-calcite mineralization on the EPS of ANME/SRB aggregates. With constant and relatively increasing methane flux, gas-bubble ebullition leads to increased seawater-derived sulfate concentrations in the shallow subsurface, creating conditions favorable for aragonite precipitation (Burton, 1993; Luff et al., 2004). We put forward that microstructure preservation was facilitated in methane seep sediments during periods of high methane flux by EPS mineralization and subsequent engulfment in aragonite cement.

Morphological resemblance and involvement in AOM

Of the three major ANME groups (ANME-1, -2, -3), ANME-1 cells typically have a cylindrical morphology (Orphan et al., 2002; Reitner et al., 2005) whereas ANME-2 and -3 often form spherical aggregates comprised of core archaeal cells surrounded by one or two layers of SRB (Boetius et al., 2000; Orphan et al., 2002; McGlynn et al., 2018). Likewise, one or two Mg-calcite layers surround the nanocrystalline cores of the spheres (Fig. 2), resembling mineralized ANME-2 aggregates with central archaea enveloped by SRB. It is noteworthy that the microstructure diameters fall in the average size range of laboratory maintained ANME-2/SRB aggregates of ~6 to ~25 µm (e.g. Nauhaus et al., 2007). The notion that the spheres represent mineralized ANME-2-*Desulfosarcina/Desulfococcus* (DSS) aggregates is supported by the lipid biomarker data. In contrast to archaea of the ANME-1 group, ANME-2 archaea are typified by *sn2*-hydroxyarchaeol to archaeol ratios >1 and the presence of crocetane (Blumenberg et al., 2004; Niemann and Elvert, 2008). The two carbonate samples yielded abundant crocetane and *sn2*-hydroxyarchaeol to archaeol ratios >2, in accord with the derivation of the biomarkers from ANME-2/*DSS* consortia (cf. Pancost et al., 2000; Blumenberg et al., 2004; Stadnitskaia et al., 2005; Niemann and Elvert, 2008). Alternatively, the microstructures could be traces of autoendolithic SD–AOM activity postdating the pore-filling aragonite. It was shown that viable aggregates of the SD–AOM-mediating microbes thrive within seep carbonates (Marlow et al., 2014; 2015). The *in situ* spatial location of autoendolithic ANME/SRB aggregates in methane seep carbonates has not yet been resolved, but it is assumed these methane oxidizing microbes are concentrated in regions with hydraulically open pore space (Marlow et al., 2015). In the case of the putative AOM-microfossils described in our study, the clustered spheres are fully engulfed in aragonite with no apparent open fractures. This indicates that the spheres must have been mineralized before they were engulfed in aragonite.

To test potential involvement of the microstructures in anaerobic methane oxidation, *in situ* $\delta^{13}C$ values of one representative sphere were analyzed. The microstructure had consistently negative $\delta^{13}C$ values (−42 to –24‰), ranging between seepage methane ($\delta^{13}C$: −63 to −45‰; Panieri et al., 2017), carbonate cement ($\delta^{13}C$: −33 to −21‰; data file DR2), and seawater dissolved inorganic carbon (DIC; ≈ 0‰; Fig. 3B). High-angle annular dark field imaging revealed that the interior nanocrystals of this sphere are immersed in a dark gray material (Figs. 2D;3A). It is interpreted as remnant organic matter associated with the sphere. Because the Mg-calcite crystals are immersed in the organics, both materials likely contribute to the secondary carbon ion signal to different degrees. The proportion of the analyzed ions derived from the carbonate relative to the organics is difficult to quantify. However, carbonate has significantly lower ionization yield relative to organics and it is reasonable to assume that most of the signal was derived from organic matter (Williford et al., 2016). In seep sediments, ^{13}C-depleted organic matter is mainly comprised by chemotrophic ANME/SRB consortia using methane as dominant carbon source for biomass production (Orphan et al., 2001). Consequently, negative microstructure $\delta^{13}C$ values as low as −42‰ point to the presence of chemotrophic biomass and are consistent with fluorescence *in situ* hybridization–SIMS $\delta^{13}C$ measurements for natural ANME/SRB consortia from seep sediments (Orphan et al., 2001; 2002; House et al., 2009). However, the microstructure $\delta^{13}C$ values are not as low as the measured values of the biomarkers (Fig. 3). This discrepancy may be explained by the mixed carbon source, comprising a mixture of relatively isotopically heavier Mg-calcite and extremely light organic matter.

CONCLUSIONS

Microscopic analyses of late Pleistocene seep carbonates recovered from an active deep sea methane seep in 1200 m water depth revealed clusters of spherical microstructures engulfed in ^{13}C-depleted aragonite cement. The spheres range in diameter between ~5 μm (single sphere)

to ~30 µm (cluster). EDX analyses performed on sphere cross-sections revealed their carbonate mineralogy with magnesium peaks but no distinct strontium. The elemental composition in concert with Fast Fourier Transform diffraction patterns indexed as rhombohedral crystal surfaces point to Mg-calcite mineralogy of the spheres. The interior of the spheres is characterized by a porous framework of Mg-calcite nanocrystals, whereas the exterior is comprised by one or two ~1 to 2 µm wide Mg-calcite layers. *In situ* carbon isotopes of one representative sphere yielded negative $\delta^{13}C$ values as low as −42‰, agreeing with involvement of the microstructures in anaerobic methane oxidation. A suite of ^{13}C-depleted archaeal and bacterial biomarkers extracted from the carbonates corroborates that carbonate precipitation was induced by microbial consortia of anaerobic methanotrophic archaea and sulfate-reducing bacteria. The biomarkers are indicative of ANME-2 archaea, which are known to form spherical aggregates surrounded by one or two layers of sulfate-reducing bacteria. Given that the microstructures are preserved in microbially-induced seep carbonates, it is put forward that the clustered spheres represent fossils of SD–AOM-mediating methanotrophic archaea and sulfate-reducing bacteria.

ACKNOWLEDGMENTS

Professional support at sea by the master and crew during expeditions P1606 on R/V G.O. Sars and skillful work of the ROV Ægir 6000 team (University of Bergen) are greatly acknowledged. Thanks to Anja Schreiber (GeoForschungsZentrum, Potsdam) for meticulous FIB work and Yunbin Guan (Caltech, Pasadena) for nanoSIMS operations. Thoughtful comments by Russell S. Shapiro and two anonymous reviewers helped to improve the manuscript. This study was supported by the Research Council of Norway through the Petromaks2 NORCRUST project (grant # 255150, 223259).

REFERENCES

Aloisi, G., Bouloubassi, I., Heijs, S.K., Pancost, R.D., Pierre, C., Sinninghe Damsté, J.S., Gottschal, J.C., Forney, L.J., and Rouchy, J.-M., 2002, CH_4-consuming microorganisms and the formation of carbonate crusts at cold seeps: Earth and Planetary Science Letters, v. 203, p. 195–203.

Bailey, J.V., Raub, T.D., Meckler, A.N., Harrison, B.K., Raub, T.M.D., Green, A.M., and Orphan, V.J., 2010, Pseudofossils in relict methane seep carbonates resemble endemic microbial consortia: Palaeogeography, Palaeoclimatology, Palaeoecology, v. 285, p. 131–142.

Blumenberg, M., Seifert, R., Reitner, J., Pape, T., and Michaelis, W., 2004, Membrane lipid patterns typify distinct anaerobic methanotrophic consortia: Proceedings of the National Academy of Sciences, v.101, p. 11111–11116.

Boetius, A., Ravenschlag, K., Schubert, C.J., Rickert, D., Widdel, F., Gieseke, A., Amann, R., Jørgensen, B.B., Witte, U., and Pfannkuche, O., 2000, A marine microbial consortium apparently mediating anaerobic oxidation of methane: Nature, v. 407, p. 623–626, doi: 10.1038/35036572.

Braissant, O., Decho, A.W., Dupraz, C., Glunk, C., Przekop, K.M., and Visscher, P.T., 2007, Exopolymeric substances of sulfate-reducing bacteria: interactions with calcium at alkaline pH and implication for formation of carbonate minerals: Geobiology, v. 5, p. 401–411.

Burton, E.A., 1993, Controls on marine carbonate cement mineralogy: review and reassessment: Chemical Geology, v. 105, p, 163–179.

Himmler, T., Sahy, D., Martma, T., Bohrmann, G., Plaza–Faverola, A., Bünz, S., Condon, D.J., Knies, J., and Lepland, A., 2019, A 160,000-year-old history of tectonically controlled methane seepage in the Arctic: Science Advances, v. 5, eaaw1450, doi: 10.1126/sciadv.aaw1450.

House, C.H., 2015, A synthetic standard for the analysis of carbon isotopes of carbon in silicates, and the observation of a significant water–associated matrix effect: Geochemical Transactions, v. 16, doi: 10.1186/s12932-015-0029-x.

House, C.H., Orphan, V.J., Turk, K.A., Thomas, B., Pernthaler, A., Vrentas, J.M., and Joye, S.B., 2009, Extensive carbon isotopic heterogeneity among methane seep microbiota: Environmental Microbiology, v. 11, p. 2207–2215.

Knittel, K., Wegener, G., and Boetius, A., 2018, Anaerobic Methane Oxidizers, in McGenity, T.J., ed., Microbial Communities Utilizing Hydrocarbons and Lipids: Members, Metagenomics and Ecophysiology: Springer International Publishing, p. 1–21, https://doi.org/10.1007/978-3-319-60063-5_7-1.

Lu, Y., Sun, X., Xu, H., Konishi, H., Lin, Z., Xu, L., Chen, T., Hao, X., Lu, H., and Peckmann, J., 2018, Formation of dolomite catalyzed by sulfate-driven anaerobic oxidation of methane: Mineralogical and geochemical evidence from the northern South China Sea: American Mineralogist, v. 103, p. 720–734.

Luff, R., Wallmann, K., and Aloisi, G., 2004, Numerical modeling of carbonate crust formation at cold vent sites: significance for fluid and methane budgets and chemosynthetic biological communities: Earth and Planetary Science Letters, v. 221, p. 337–353.

Marlow, J.J., Steele, J.A., Ziebis, W., Thurber, A.R., Levin, L.A., and Orphan, V.J., 2014, Carbonate-hosted methanotrophy represents an unrecognized methane sink in the deep sea: Nature Communications, v. 5, 5094, doi: 10.1038/ncomms6094.

Marlow, J.J., Peckmann, J., and Orphan, V.J., 2015, Autoendoliths: a distinct type of rock-hosted microbial life: Geobiology, v. 13, p. 303–307, https://doi.org/10.1111/gbi.12131.

McGlynn, S.E., Chadwick, G.L., O'Neill, A., Mackey, M., Thor, A., Deerinck, T.J., Ellisman, M.H., and Orphan, V.J., 2018, Subgroup characteristics of marine methane-oxidizing ANME-2 archaea and their syntrophic partners as revealed by integrated multimodal

247 analytical microscopy: Applied and Environmental Microbiology, v. 84, pp.e00399-18, doi:
248 10.1128/AEM.00399-18.
249 Michaelis, W., Seifert, R., Nauhaus, K., Treude, T., Thiel, V., Blumenberg, M., Knittel, K.,
250 Gieseke, A., Peterknecht, K., Pape, T., Boetius, A., Amann, R., Jørgensen, B.B., Widdel, F.,
251 Peckmann, J., Pimenov, N.V., and Gulin, M.B., 2002, Microbial reefs in the Black Sea
252 fueled by anaerobic oxidation of methane: Science, v. 297, p. 1013–1015.
253 Niemann, H., and Elvert, M., 2008, Diagnostic lipid biomarker and stable isotope signatures of
254 microbial communities mediating the anaerobic oxidation of methane with sulphate:
255 Organic Geochemistry, v. 39, p. 1668–1677, doi:10.1016/j.orggeochem.2007.11.003.
256 Nauhaus, K., Albrecht, M., Elvert, M., Boetius, A., and Widdel, F., 2007, In vitro cell growth of
257 marine archaeal-bacterial consortia during anaerobic oxidation of methane with sulfate:
258 Environmental Microbiology, v. 9, p. 187–196. doi:10.1111/j.1462-2920.2006.01127.x.
259 Orphan, V.J., House, C.H., Hinrichs, K.-U., McKeegan, K.D., and DeLong, E.F., 2001, Methane-
260 consuming archaea revealed by directly coupled isotopic and phylogenetic analysis:
261 Science, v., 293, p. 484–487.
262 Orphan, V.J., House, C.H, Hinrichs, K.-U., McKeegan, K.D., and DeLong, E.F., 2002, Multiple
263 archaeal groups mediate methane oxidation in anoxic cold seep sediments: Proceedings of
264 the National Academy of Sciences, v. 99, p. 7663–7668, doi: 10.1073/pnas.072210299.
265 Pancost, R.D., Hopmans E.C., Sinninghe Damsté, J.S., and the Medinaut shipboard scientific
266 party, 2001, Archael lipids in Mediterranean cold seeps: molecular proxies for anaerobic
267 methane oxidation: Geochimica et Cosmochimica Acta, v. 65, p. 1126–1132, doi:
268 10.1016/S0016-7037(00)00562-7.
269 Panieri, G., Bünz, S., Fornari, D.J., Escartin, J., Serov, P., Jansson, P., Torres, M.E., Johnson,
270 J.E., Hong, W., Sauer, S., Garcia, R., and Gracias, N., 2017, An integrated view of the

methane system in the pockmarks at Vestnesa Ridge, 79°N: Marine Geology, v. 390, p. 282–300, http://dx.doi.org/10.1016/j.margeo.2017.06.006.

Peckmann, J., and Thiel, V., 2004, Carbon cycling at ancient methane seeps: Chemical Geology, v. 205, p. 443–467.

Reitner, J., Peckmann, J., Blumenberg, M., Michaelis, W., Reimer, A., and Thiel, V., 2005, Concretionary methane-seep carbonates and associated microbial communities in Black Sea sediments: Palaeogeography, Palaeoclimatology, Palaeoecology, v. 227, p. 18– 30.

Rouillard, J., van Zuilen, M., Pisapia, C., and Garcia-Ruiz, J.M., 2021, An alternative approach for assessing biogenicity: Astrobiology, v. 21, p. 151–164, doi: 10.1089/ast.2020.2282.

Shapiro, R.S., 2004, Recognition of fossil prokaryotes in Cretaceous methane seep carbonates: relevance to astrobiology: Astrobiology, v. 4, p. 438–449.

Suess, E., 2018, Marine cold seeps: background and recent advances, in Wilkes, H., ed., Hydrocarbons, Oils and Lipids: Diversity, Origin, Chemistry and Fate: Springer International Publishing, p. 1–21, doi: 10.1007/978-3-319-54529-5_27-1.

Stadnitskaia, A., Muyzer, G., Abbas, B., Coolen, M.J.L., Hopmans, E.C., Baas, M., van Weering, T.C.E., Ivanov, M.K., Poludetkina, E., and Sinninghe Damsté, J.S., 2005, Biomarker and 16S rDNA evidence for anaerobic oxidation of methane and related carbonate precipitation in deep-sea mud volcanoes of the Sorokin Trough, Black Sea: Marine Geology, v. 217, p.67–96.

Slodzian, G., Hillion, F., Stadermann F.J., and Zinner E., 2004, QSA influences on isotopic ratio measurements: Applied Surface Science, v. 231–232, p. 874–877, doi: 10.1016/j.apsusc.2004.03.155.

Wirth, R., 2009, Focused ion beam (FIB) combined with SEM and TEM: advanced analytical tools for studies of chemical composition, microstructure and crystal structure in

geomaterials on a nanometre scale: Chemical Geology, v. 261, p. 217–229, doi: 10.1016/j.chemgeo.2008.05.019.

Williford, K.H., Ushikubo, T, Lepot, K., Kitajima, K., Hallmann, C., Spicuzza, M.J., Kozdon, R., Eigenbrode, J.L., Summons, R.E., and Valley, J.W., 2016, Carbon and sulfur isotopic signatures of ancient life and environment at the microbial scale: Neoarchean shales and carbonates: Geobiology, vol. 14, p. 105–128, doi: 10.1111/gbi.12163.

Zhang, F., Xu, H., Konishi, H., Kemp, J.M., Roden, E.E., and Shen, Z., 2012, Dissolved sulfide catalyzed precipitation of disordered dolomite: implications for the formation mechanism of sedimentary dolomite: Geochimica et Cosmochimica Acta, v. 97, p. 148–165.

FIGURE CAPTIONS

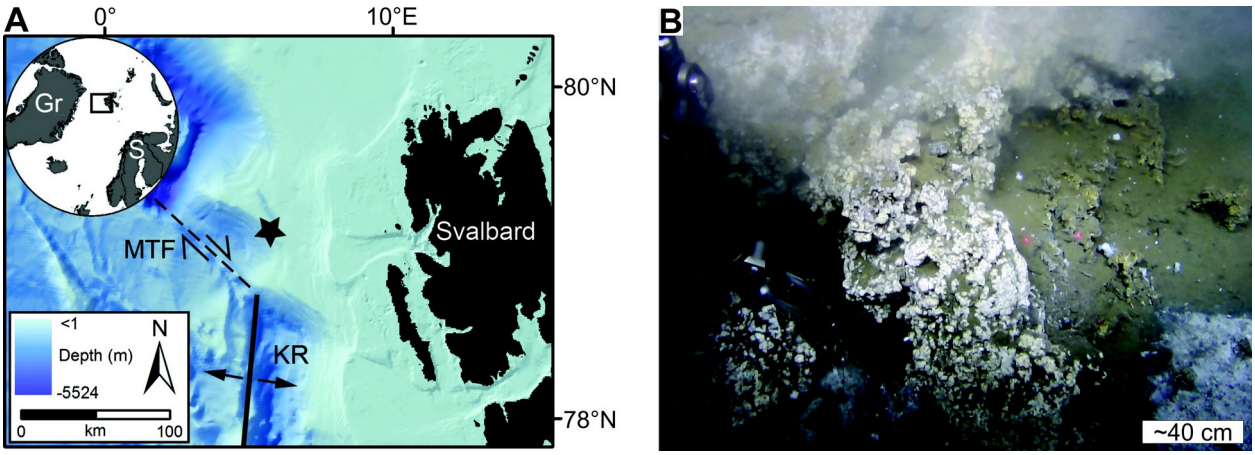

Figure 1. Sample location and seabed image. A: Bathymetry and tectonic setting; seep carbonates were sampled at 79° 0.1445'N, 06° 55.389'E (P1606001) and 79° 0.156'N, 06° 55.278'E (P1606002); asterisk—sampling location in ~1200 m water depth; Gr—Greenland; S—Scandinavia; KR—Knipovich Ridge; MTF—Molloy Transform Fault. B: Seafloor image; carbonates (light) partly draped with brownish sediment; note colorless microbial mats lower left and right indicative of active methane seepage.

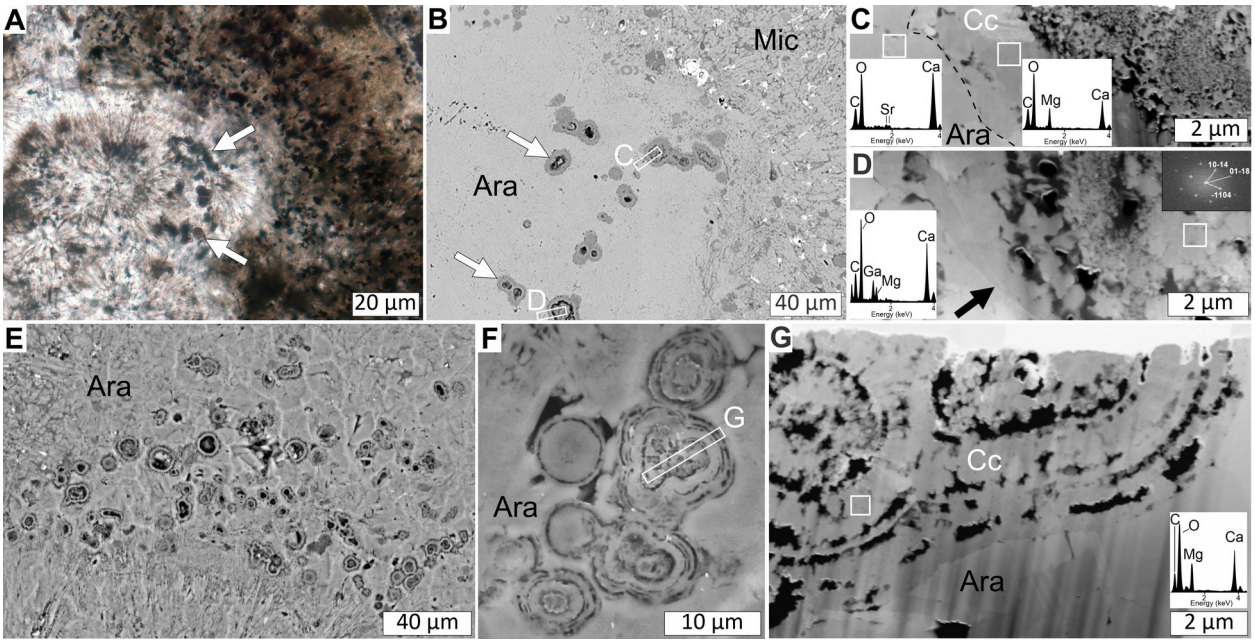

Figure 2. Microstructure SEM- and TEM-images (HAADF: high-angle annular dark field; pore space appears black) showing the structural and elemental compositions (A–E—sample P1606001; F–G—sample P1606002). A: Thin section micrograph (transmitted parallel polarized light); arrows point to clusters engulfed in aragonite cement. B: SEM-image of clustered Mg-calcite spheres (arrows); note relatively lower (dark gray) backscatter signal of the spheres compared to the surrounding cement (light gray) due to the relatively higher abundance of magnesium (Mg^{2+}) and strontium (Sr^{2+}); Ara—aragonite; Mic—microcrystalline aragonite cemented sediment; rectangles depict TEM-foils shown in C and D. C,D,G: HAADF-images showing sphere cross sections (top image—surface); calcium carbonate appears light gray; note porous central part (right); squares—EDX analyses, insets left and center show respective spectra; inset upper right in D shows representative Fast Fourier transform pattern of lattice fringes observed in the core, indexed as rhombohedral crystal faces {10−14}, {10−18}, and {−1104}; note, relatively high Mg indicate Mg-calcite (Cc), elevated strontium (Sr) aragonite (Ara); Ga peak from redeposited material from FIB milling; dashed line in C—Mg-calcite–aragonite contact; arrow in D depicts hole in carbon grid carrying foil. E: SEM-image of clusters

after surface ion milling; Ara—aragonite. F: SEM-image showing clustered spheres engulfed in aragonite (Ara); rectangle depicts TEM-foil shown in G. G: HAADF-image of clustered spheres with concentric outer layers and porous interiors.

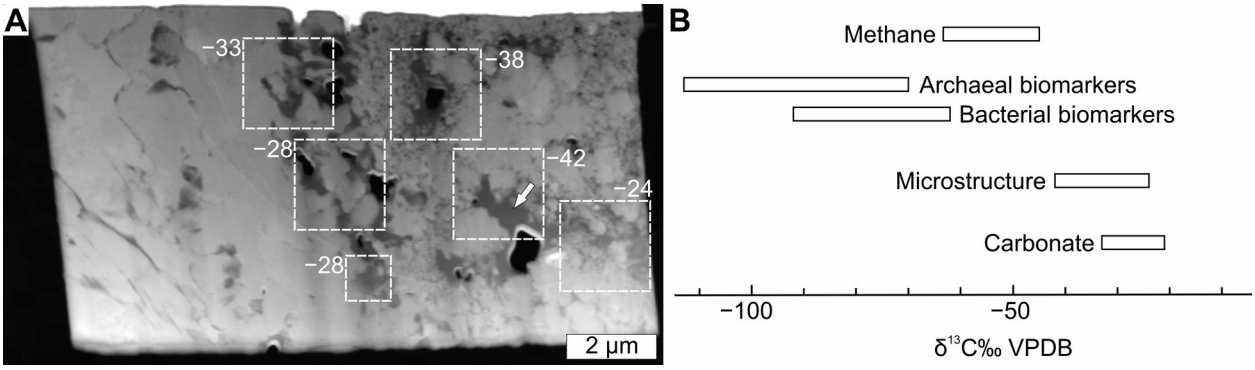

Figure 3. NanoSIMS $\delta^{13}C$ spot analyses and $\delta^{13}C$ values compilation. A: HAADF-image of single sphere cross section; dashed squares depict areas of nanoSIMS analyses; numbers are corrected $\delta^{13}C$nanoSIMS values (see Data Repository for details); arrow points to dark gray material which surrounds Mg-calcite crystals. B: Compiled $\delta^{13}C$ ranges; $\delta^{13}C_{methane}$ adopted from Panieri et al. (2017); $\delta^{13}C_{microstructure}$ shown after QSA-correction; $\delta^{13}C_{carbonate}$ adopted from Himmler et al. (2019).

[1]GSA Data Repository item 201Xxxx, with detailed methods, supplementary figures showing microfacies context of microstructures and nanoSIMS data correlation plots, as well as supplemental data file including nanoSIMS data, lipid biomarker data, mineralogy, and carbonate stable carbon and oxygen isotope compositions is available online at www.geosociety.org/pubs/ft20XX.htm, or on request from editing@geosociety.org or Documents Secretary, GSA, P.O. Box 9140, Boulder, CO 80301, USA.

Putative fossils of chemotrophic microbes preserved in seep carbonates from Vestnesa Ridge, off northwest Svalbard, Norway
Himmler et al.

SUPPLEMENTAL MATERIAL

METHODS

Thin section microscopy

Polished thin sections (~30 µm thickness, 6.5 x 5 cm) were prepared from carbonate slabs embedded in epoxy resin and were examined using scanning electron microscopy (Zeiss Leo 1450 VP; 15 kV; ~11 and ~15 mm working distance; variable pressure) and transmitted light microscopy (Zeiss Axioplan2 equipped with an AxioCam ERc 5s digital camera; Figs. S1 and S4).

Thin section surface polishing

Thin section surfaces with abundant clustered microstructures were polished using a Leica EM RES102 argon (Ar) ion milling system, applying an Ar plasma at 8 kV for approximately 1 hour (3 degrees incidence angle) for surface leveling, followed by milling at 4 kV for approximately 1 hour (15 degrees incidence angle) for cleaning (Fig. S4).

Mineralogy

Quantitative mineralogical composition was determined by X-ray diffraction on powders obtained with a hand-held microdrill from cut slab surfaces (Data file S1). Powders were analyzed using a Bruker D8 Advance diffractometer using copper K-α radiation at a 2Θ scanning angle of 3° to 75° (step size of 0.02°, 1 s per step). Minerals were identified by automatic and manual peak search using the Bruker Diffrac EVA 5.2 software; quantification was performed applying Rietveld refinement using TOPAS 5.0 software (2 to 3 weight-% uncertainty).

Lipid biomarker and compound-specific carbon isotope analyses

Two cut slabs of carbonate samples P1606001 and P1606002 were prepared for lipid biomarker analysis. The slabs were cleaned with deionised water and the exterior surfaces were removed with hammer and chisel. The remaining sample material was cleaned with acetone and crushed to small nugget-sized pieces. Dissolution of the carbonate matrix of the nugget-sized pieces was done by slowly pouring 10% hydrochloric acid onto them. After ca. 75% of the carbonate was dissolved, the hydrochloric acid solution was discarded. The remaining sediment was collected, saponified and extracted. To release ester-bond carboxylic acids, the sample was

treated with 6% KOH in methanol (base hydrolysis). The reaction was done in a 100 ml screw-cap vial in an ultrasonic bath at 80°C for 2 hours. The saponification extract was collected in a separatory funnel. In the following, the samples were extracted three times with a mixture of dichloromethane and methanol (3:1). The samples were ultrasonicated for 15 minutes at ambient temperature. After each extraction, the dichloromethane and methanol mixture was combined with the saponification extract in the separatory funnel. Then, demineralized water was added, the aqueous phase was acidified to release the fatty acid salts and transfer them as free fatty acids to the organic phase. The combined total lipid extract (TLE) was collected in a round flask and dried to near dryness with a rotation evaporator. An aliquot of the TLE was further separated in *n*-hexane soluble maltenes and dichloromethane-soluble asphaltenes. The maltenes were separated with an aminopropyl-modified silica gel column into four fractions with increasing polarity (Birgel et al., 2008). Only hydrocarbon, alcohol, and carboxylic acid fractions contained indigenous compounds, the ketone fraction is not further discussed. Alcohols and carboxylic acids were derivatized with N,O-bis(trimethylsilyl)fluoracetamide (BSTFA) and pyridine (1:1) and 10% BF_3 in methanol for 1 hour at 80°C, respectively. All samples were analyzed with a GC-MS (Thermo Electron Trace GC Ultra) coupled to a Thermo Electron DSQ II mass spectrometer with a DB-5 MS ultra inert column (30 m; 0.25 mm inner diameter, 0.25 mm film thickness). The temperature program was 50°C (3 min), then with 8°C/min to 325°C. The final temperature was held for 20 minutes. Carrier gas on the GC-MS was helium. Compound-specific carbon isotopes were measured on a gas chromatograph (Agilent 6890) coupled with a Thermo Finnigan Combustion III interface to a Finnigan Delta Plus XL isotope ratio mass spectrometer (GC-IRMS). The GC conditions were identical to those of the GC-MS. The alcohols and carboxylic acids were corrected for the addition of carbon atoms during derivatization. The samples were measured in duplicate and the standard deviation of the isotope measurements was below 0.8‰ and was determined with a Schimmelmann reference Standard Mixture B. Quantification of compounds was done via internal standards added prior saponification.

Focused ion beam–transmission electron microscopy (FIB–TEM)

FIB-foils for TEM analyses were prepared under ultrahigh vacuum oil-free conditions using the FEI FIB 200TEM instrument at the GeoForschungsZentrum Potsdam, Germany. The foils are approximately 15×10×0.150 µm (length, height, thickness) in dimension. Foils were milled from a thin section and a polished rock sample with a gallium (Ga^{2+}) ion beam at 30 kV acceleration voltage. Subsequently, the foils were placed on a holey carbon film which was

mounted on a copper grid sample holder. Carbon coating was omitted. Electron conductivity was induced by implantation of a thin layer of Ga^{2+}–ions into the sample surface (Wirth, 2009). Prior to TEM analyses potential surface contaminations were removed using a plasma (25 vol.% oxygen, 75 vol.% argon) cleaner for about 10 seconds. TEM was carried out on a FEI Tecnai G2 F20 X-Twin transmission electron microscope. Elemental compositions were measured with an EDX energy dispersive X-ray spectroscopy system.

Nanoscale secondary ion mass spectrometry (nanoSIMS) $\delta^{13}C$ analyses

The nanoSIMS $\delta^{13}C$ analyses were done on a gold-coated (~30 nm) TEM-foil milled from a thin section, using the CAMECA NanoSIMS 50L instrument at the Division of Geological and Planetary Sciences, California Institute of Technology, U.S.A. Prior to measurements, areas of interest were sputtered using a primary cesium (Cs^+) beam for approximately five minutes to locally remove the coating. Signals of $^{12}C^-$, $^{13}C^-$, and $^{40}Ca^{2+}$ ions were collected on electron multipliers with the electron gun for charge compensation, at a stable primary column current (current not recorded) over 1x1 and 2x2 µm square regions on the sample and the standard material (Data file S1). Ceramacast 905 (C-905), a synthetic standard containing organic carbon in a silicate matrix (House, 2015), was repeatedly measured before and after sample analyses. Average uncertainty for individual $\delta^{13}C$ analyses (1σ) was calculated at 5.3‰ (n = 6; Data file S1).

During standard measurements monitoring $^{13}C/^{12}C$ and ^{12}C counts, a positive linear correlation was observed (Fig. S2A). The correlation suggests a quasi-simultaneous arrival (QSA) effect. The QSA effect occurs when a single incoming primary ion produces multiple secondary ions that are recorded by the electron multipliers as a single event (Slodzian et al., 2004). As a result, the recorded counts for the major isotope (i.e. ^{12}C) are lower than the actual emitted secondary $^{12}C^-$ ions and thus the calculated $^{13}C/^{12}C$ ratio becomes artificially higher with increasing counts. In order to rule out other potential analytical artifacts influencing $^{13}C/^{12}C$ and ^{12}C signal relationships, such as heterogeneity of C-905, a homogeneous graphite standard (unknown $\delta^{13}C$) was studied in a follow-up session. By changing the slit aperture at a constant primary column current (25 nA), a similar positive linear correlation was observed (Fig. S2B).

Correction for QSA was done following Slodzian et al. (2004) (excluding 2σ outliers) and instrumental mass fractionation (IMF) was determined on the working standard (N = 22) using the following equation:

$$\alpha_{IMF} = \frac{(1000 + \delta^{13}C_{QSA})}{(1000 + \delta^{13}C_{true})}$$

where $\delta^{13}C_{QSA}$ is the QSA-corrected value and $\delta^{13}C_{true}$ was assumed −27.9‰ VPDB for the standard material (House, 2015). The calculated α_{IMF} is 0.963 (σ_{IMF} = 3.4‰, n=8). This IMF was then applied to correct each individual sample analysis using the same equation. The total uncertainty for each measurement is calculated as following (House et al., 2013)

$$\sigma_{tot.} = \sqrt{\sigma_{\int .}^2 + \sigma_{IMF}^2}$$

where $\sigma_{int.}$ is the internal error of each analysis spot and σ_{IMF} is the mean IMF standard error calculated after QSA correction. Uncertainties for sample $\delta^{13}C$ analyses (1σ) ranged from 3.9 to 8.1 ‰, averaging at 5.1‰ (n = 6; Data file S1). Figure S3 compares $\delta^{13}C$ values corrected and non-corrected for QSA effect.

SUPPLEMENTARY FIGURES

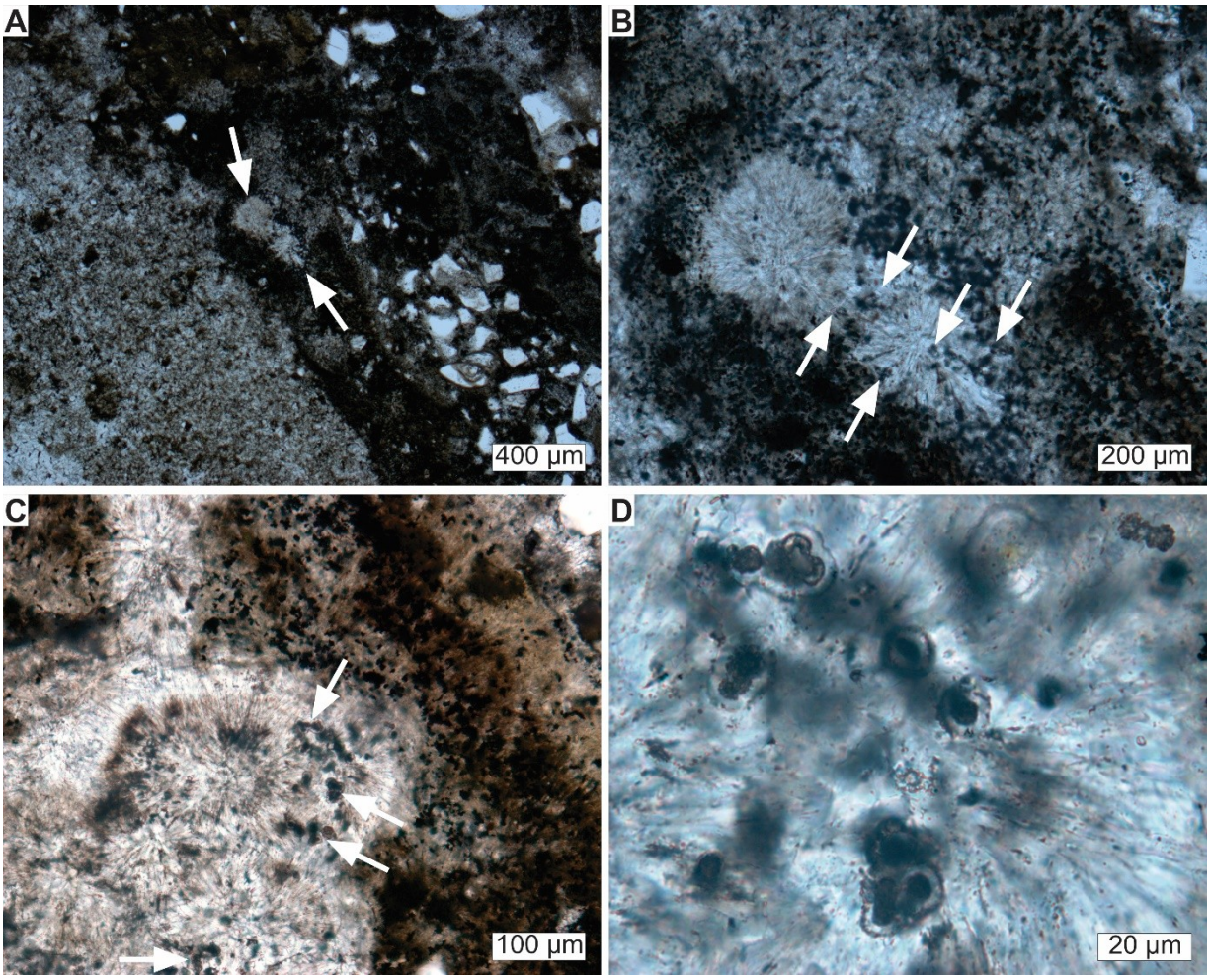

Figure S1. Thin section micrographs of microstructures (sample P1606001; parallel-polarized transmitted light). (A) Voids filled with aragonite (arrows) in inclusion-rich cement at the border to micrite-cemented sediment containing silt-sized quartz (right). (B to D) Magnified views of void-filling aragonite with microstructures (arrows); note distinct calcite layer around spheres in D.

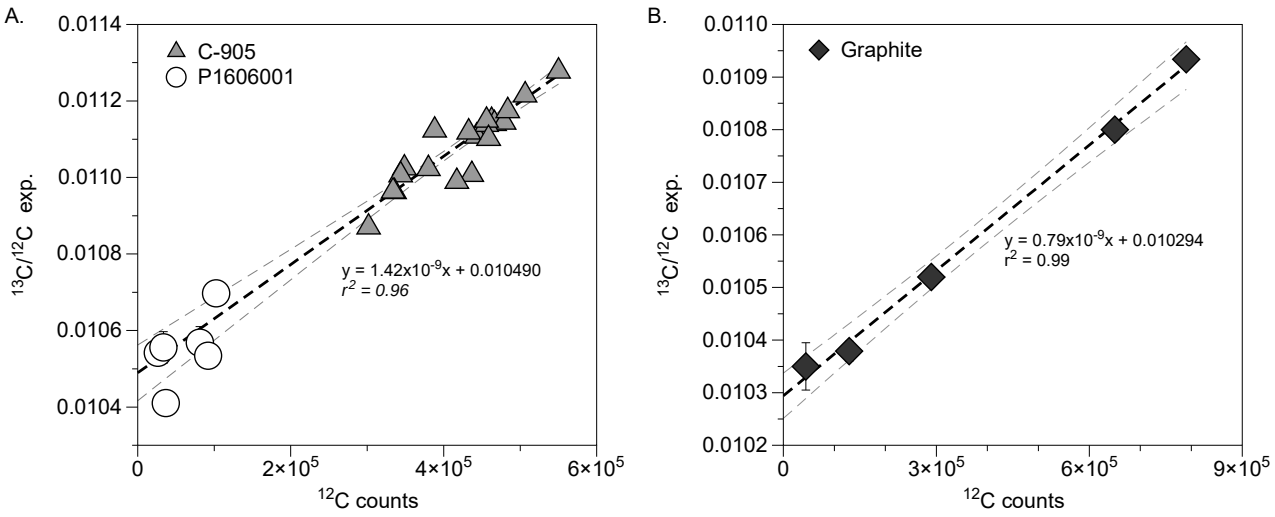

Figure S2. Correlations between experimental (exp.) $^{13}C/^{12}C$ and ^{12}C counts. (A) Standard C-905 (N = 22) and sample analyses. (B) Graphite standard; error bars are 1σ internal precision ($\sigma_{int.}$) for each analysis spot.

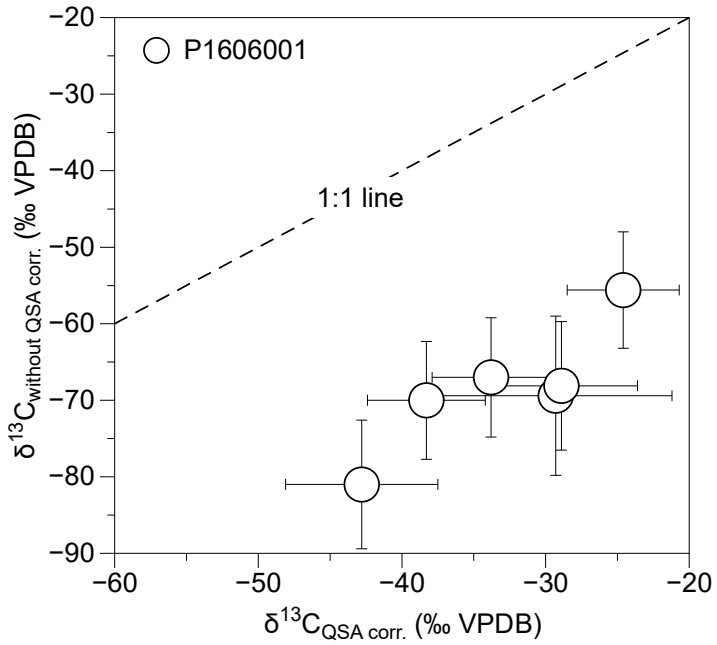

Figure S3. Relationship between sample $\delta^{13}C$ values corrected and non-corrected for QSA; error bars are total uncertainty ($\sigma_{tot.}$) calculated for each analysis spot.

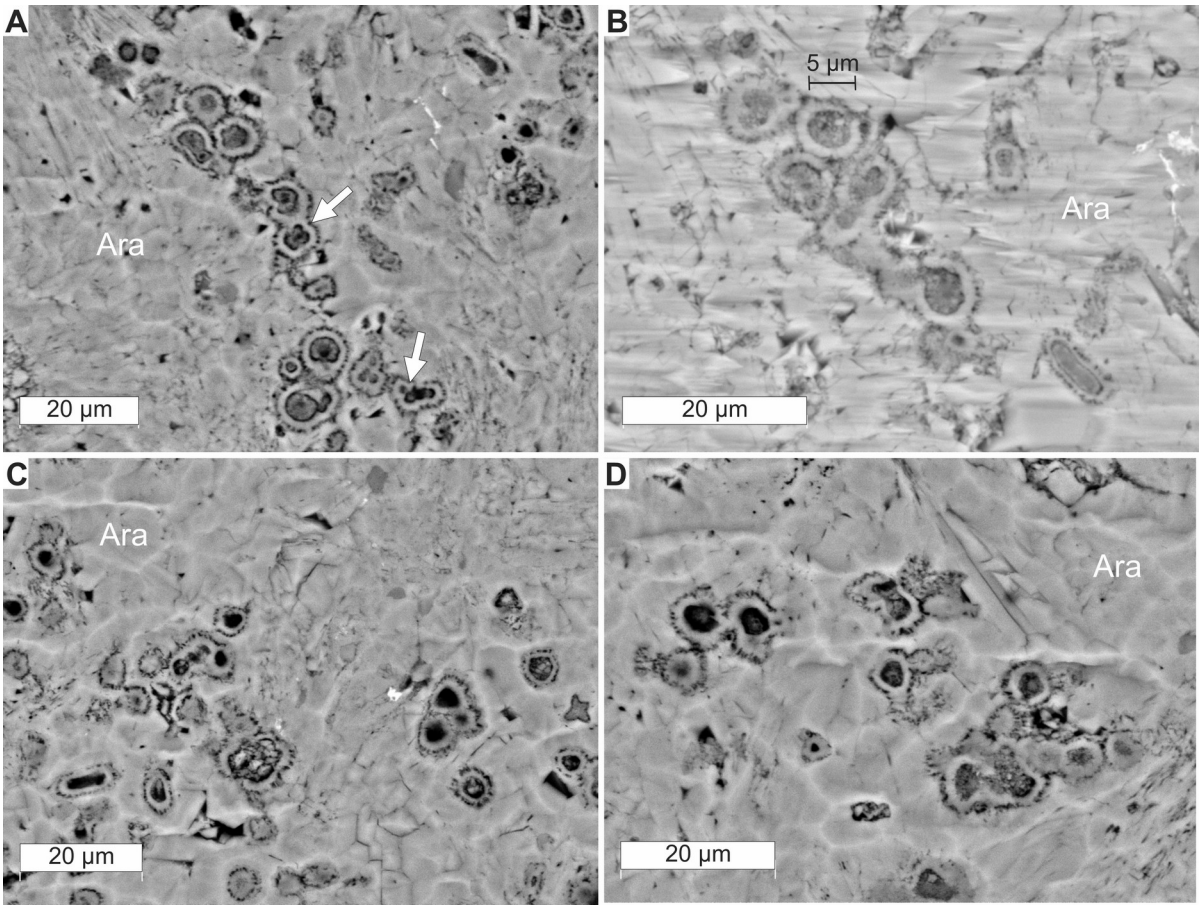

Figure S4. Thin section backscatter scanning electron microscope images showing microfacies context of clustered spheres engulfed in aragonite cement (Ara). (A) Clusters engulfed in aragonite; note areas where spheres invaginate (arrows), typical when ANME/SRB consortia divide by SRB growing into the archaeal core (Knittel et al., 2018). (B) Ion-milled surface showing cluster and size of individual sphere. (C, D) Examples of clusters and individual spheres enclosed by aragonite (Ara).

References

Birgel, D., Elvert, M., Han, X., and Peckmann, J., 2008, ^{13}C-depleted biphytanic diacids as tracers of past anaerobic oxidation of methane: Organic Geochemistry, v. 39, p. 152–156.

House, C.H., 2015, A synthetic standard for the analysis of carbon isotopes of carbon in silicates, and the observation of a significant water-associated matrix effect: Geochemical Transactions, v. 16, DOI 10.1186/s12932-015-0029-x.

House, C.H., Oehler, D.Z., Sugitani, K., and Mimura, K., 2013, Carbon isotopic analyses of ca. 3.0 Ga microstructures imply planktonic autotrophs inhabited Earth's early oceans: Geology, v. 41, p. 651–654.

Knittel, K., Wegener, G., and Boetius, A., 2018, Anaerobic Methane Oxidizers, *in* McGenity, T.J., ed., Microbial Communities Utilizing Hydrocarbons and Lipids: Members, Metagenomics and Ecophysiology: Springer International Publishing, p. 1–21, https://doi.org/10.1007/978-3-319-60063-5_7-1.

Slodzian, G., Hillion, F., Stadermann F.J., and Zinner E., 2004, QSA influences on isotopic ratio measurements: Applied Surface Science, vol. 231–232, p. 874–877, doi: 10.1016/j.apsusc.2004.03.155.

Wirth, R., 2009, Focused ion beam (FIB) combined with SEM and TEM: advanced analytical tools for studies of chemical composition, microstructure and crystal structure in geomaterials on a nanometre scale: Chemical Geology, v. 261, 217–229, doi:10.1016/j.chemgeo.2008.05.019.